Title	Catalytic mechanism of the dehydrogenation of ethylbenzene over Fe-Co/Mg(Al)O derived from hydrotalcites
Author(s)	Tope, Balkrishna B.; Balasamy, Rabindran J.; Khurshid, Alam; Atanda, Luqman A.; Yahiro, Hidenori; Shishido, Tetsuya; Takehira, Katsuomi; Al-Khattaf, Sulaiman S.
Citation	Applied Catalysis A-General , 407 (1-2) : 118 - 126
Issue Date	2011
DOI	10.1016/j.apcata.2011.08.032
Self DOI	
URL	https://ir.lib.hiroshima-u.ac.jp/00034822
Right	(c) 2012 Elsevier B.V. All rights reserved.
Relation	

Catalytic mechanism of the dehydrogenation of ethylbenzene over Fe–Co/Mg(Al)O derived from hydrotalcites

Balkrishna B. Tope, Rabindran J. Balasamy, Alam Khurshid, Luqman A. Atanda, Hidenori Yahiro[1], Tetsuya Shishido[2], Katsuomi Takehira*[3], Sulaiman S. Al-Khattaf*

KAUST Center in Development, King Fahd University of Petroleum and Minerals, Dhahran 31261, Saudi Arabia.

Corresponding author. Tel.: +966 3 860 1429; Fax: +966 3 860 4234.
E-mail addresses: takehira@hiroshima-u.ac.jp (K. Takehira), skhattaf@kfupm.edu.sa (S.S. Al-Khattaf).
[1] Department of Materials Science and Biotechnology, Graduate School of Science and Engineering, Ehime University, Matsuyama 790-8577, Japan
[2] Department of Molecular Engineering, Graduate School of Engineering, Kyoto University, Nishikyo-ku, Kyoto 615-8510, Japan.
[*3] Permanent address: Professor Emeritus, Department of Applied Chemistry, Graduate School of Engineering, Hiroshima University, Higashi-Hiroshima, 739-8527, Japan.

Abstract

Catalytic mechanism of ethylbenzene dehydrogenation over Fe-Co/Mg(Al)O derived from hydrotalcites has been studied based on the XAFS and XPS catalyst characterization and the FTIR measurements of adsorbed species. Fe-Co/Mg(Al)O showed synergy, whereas Fe-Ni/Mg(Al)O showed no synergy, in the dehydrogenation of ethylbenzene. Ni species were stably incorporated as Ni^{2+} in the regular sites in periclase and spinel structure in the Fe-Ni/Mg(Al)O. Contrarily, Co species exists as a mixture of Co^{3+}/Co^{2+} in the Fe-Co/Mg(Al)O and was partially isolated from the regular sites in the structures with increasing the Co content. Co addition enhanced Lewis acidity of Fe^{3+} active sites by forming Fe^{3+}–O–$Co^{3+/2+}$(1/1) bond, resulting in an increase in the activity. FTIR of ethylbenzene adsorbed on the Fe-Co/Mg(Al)O clearly showed formations of C–O bond and π-adsorbed aromatic ring. This suggests that ethylbenzene was strongly adsorbed on the Fe^{3+} acid sites via π-bonding and the dehydrogenation was initiated by α-H^{+} abstraction from ethyl group on Mg^{2+}–O^{2-} basic sites, followed by C–O–Mg bond formation. The α-H^{+} abstraction by O^{2-}(–Mg^{2+}) was likely followed by β-H abstraction, leading to the formations of styrene and H_2. Such catalytic mechanism by the Fe^{3+} acid–O^{2-}(–Mg^{2+}) base couple and the Fe^{3+}/Fe^{2+} reduction-oxidation cycle was further assisted by Co^{3+}/Co^{2+}, leading to a good catalytic activity for the dehydrogenation of ethylbenzene.

Key words: ethylbenzene dehydrogenation; styrene, Fe^{3+}–O–$Co^{3+/2+}$(1/1) active species; hydrotalcite; EXAFS; FTIR; C–O bond formation.

1. Introduction

Styrene, an important basic chemical as a raw material for polymers, is produced commercially by the dehydrogenation of ethylbenzene using an Fe–K oxide catalyst in the presence of a large amount of superheated steam at 600–700 °C [1]. Steam affords the heat to shift the chemical equilibrium of the endothermic reaction toward higher conversion to styrene [2], assists the formation of active $KFeO_2$ species [3] and suppresses the formation of coke on the catalyst [4]. However, one should notice that steam is used in a large excess molar amount with respect to ethylbenzene (6–13:1), leading to a huge amount of energy consumption (1.5×10^6 kcal/styrene ton) [5]. Moreover, the commercial Fe-K oxide catalyst has some disadvantages: unstable active Fe^{3+} sites [6], small surface area and the migration and loss of potassium promoter [7-9].

The search for new catalysts which have large surface areas and can stabilize the active state of iron, in the absence of potassium and steam, is much needed. Aluminum was proved to be an excellent promoter, preventing sintering in iron-oxide catalysts [10]. MgO had especially good characteristics as an additive among a series of alkaline earth oxides [11]. Mg^{2+} ions possess a small ionic radii leading to a high electrostatic potential due to the stable valence state, resulting in an effective suppression of Fe sintering due to the reduction of $Fe^{3+/2+}$ to Fe^0. The author previously reported that Fe/Mg(Al)O catalyst derived from hydrotalcite showed a high activity in the dehydrogenation of ethylbenzene in the absence of steam [12]. The active Fe species exists as metastable Fe^{3+} on the Fe/Mg(Al)O catalyst. Recently the authors published

three papers: in the first paper [13], Fe–Co/Mg(Al)O bimetallic catalyst showed the highest activity in the steamless dehydrogenation of ethylbenzene among a series of Fe–Me/Mg(Al)O (Me = Cu, Zn, Cr, Mn, Fe, Co and Ni) systems. The active Fe^{3+} species was reduced at a low temperature by the Fe–Co bimetal formation in TPR, leading to the high activity. Simultaneously, the amount of reducible Fe^{3+} was the smallest, resulting in a high stability of the active Fe^{3+} species against the reduction to Fe^{0}. In the second paper [14], bimetallic Fe–Co system showed a clear synergy, i.e., the highest activity was obtained at x = 0.25 among $Fe_{0.5-x}$–Co_x/$Mg_3(Al_{0.5})O$ (x = 0–0.5), whereas Fe–Ni bimetallic system prepared as comparison showed no synergy. The dehydrogenation on the active Fe^{3+} sites was accelerated by a reduction-oxidation between Fe^{3+} and Fe^{2+} and Co assisted the reduction-oxidation by forming Fe–Co (1/1) bimetallic active species. In the third paper [15], the activity increased with increasing the Mg content in $Fe_{0.5}/Mg_{3-x}Zn_x(Al_{0.5})O$ (x = 0–3). Both CO_2-TPD and IR spectroscopy of adsorbed CO_2 clearly showed the presence of base sites, Mg^{2+}–O^{2-}, on the catalysts. The combination of Mg^{2+}–O^{2-} and Fe^{3+} was essential for the catalytic activity; the dehydrogenation of ethylbenzene was initiated by the H^+ abstraction on Mg^{2+}–O^{2-} basic sites near the Fe^{3+} sites.

In the present paper, we report further detailed characteristics of the active Fe–Co bimetallic species on Fe–Co/Mg(Al)O catalyst obtained by XPS and XAFS analyses, and FTIR measurements of pyridine adsorbed on the catalysts. It was clarified that Co exists as $Co^{3+/2+}$ mixed valence state, whereas Ni as Ni^{2+} in Fe-Ni/Mg(Al)O, although both Co^{2+} and Ni^{2+} salts were used for the catalyst preparation. Moreover, some new mechanistic features of the dehydrogenation are proposed based on the FTIR

observation of reaction intermediate possessing C–O bond in ethylbenzene adsorbed on Fe–Co/Mg(Al)O.

2. Experimental

2.1. Fe/Mg(Al)O-based catalysts' preparation

The catalysts, $Fe_{0.5-x}$–$Co_x/Mg_3(Al_{0.5})O$ (x = 0, 0.25 and 0.5), Fe_y–$Co_y/Mg_3(Al_{0.5})O$ (y = 0.1 and 0.5), $Fe_{0.5-z}$–$Ni_z/Mg_3(Al_{0.5})O$ (z = 0.25 and 0.5) and $Fe_{0.5}/Mg_3(Al_{0.5})O$ were prepared by coprecipitation of metal nitrates, followed by calcination at 550 °C [13]. An aqueous solution of the appropriate combination of the nitrates of Mg^{2+}, Zn^{2+}, Fe^{3+}, Co^{2+}, Ni^{2+} and Al^{3+} (ca. 0.05 total mol/200 ml) was added slowly with vigorous stirring into an aqueous solution of sodium carbonate (0.04 mol/400 ml). The pH of the solution was adjusted at 10.0 by dropping a 1 M aqueous solution of sodium hydroxide, leading to a precipitation of heavy slurry. After the solution was aged at 60 °C for 24 h, the precipitates were filtrated, washed with de-ionized water (1000 ml), dried in air at 100 °C for 4 h, and calcined at 550 °C for 12 h in a muffle furnace in a static air atmosphere. The concentration of Na^+ in the catalysts after the calcination was confirmed to be below 10 ppm by atomic absorption (AA).

2.2. Characterizations of catalysts.

The catalyst precursors and the catalysts were characterized by AA, powder X-ray

diffraction (XRD), nitrogen adsorption-desorption (N_2 absorption-desorption), X-ray photoelectron spectroscopy (XPS), X-ray absorption spectroscopy (XAFS) and Fourier-transformed infrared spectroscopy (FTIR).

AA measurements were carried out with a Perkin Elmer AAnalyst 100 using a mixed gas of acetylene–N_2O–air.

XRD was recorded on a Mac Science MX18XHF-SRA powder diffractometer with monochromatized CuKα radiation (λ = 0.154 nm) at 40 kV and 30 mA. The diffraction pattern was identified through comparison with those included in the JCPDS (Joint Committee of Powder Diffraction Standards) database.

N_2 adsorption-desorption isotherms at –196 °C were measured using a conventional volumetric apparatus (Bel Japan, BELSORP Mini). Before adsorption measurements, samples (ca. 0.1 g) were heated at 400 °C for 10 h under N_2 flow. Surface areas were calculated by the Brunauer-Emmett-Teller (BET) method.

XPS measurements were performed on a Perkin Elmer 1600E spectrometer using Mg Kα radiation as excitation source. In charge-up correction, the calibration of binding energy (BE) of the spectra was referenced to the C 1s electron bond energy corresponding to graphitic carbon at 284.5 eV. In addition, relative atomic sensitivity factors (ASF) were used to determine practically more accurate chemical compositions on the surface.

X-ray absorption spectroscopic measurements were performed at room temperature in a transmission mode at the EXAFS facilities installed at the BL01B1 line of SPring-8 JASRI, Harima, Japan, using a Si(1 1 1) monochrometer. The data were collected in a quick-XAFS mode. Data reduction was carried out with REX2000

ver.2.5.9 program [16]. The sample was mixed with boron nitride as a binder and then pressed into a disk (10 mm in diameter). Energy was calibrated with Cu *K*-edge absorption (8981.0 eV); the energy step for measurement in the XANES region was 0.3 V. The adsorption was normalized to 1.0 at an energy position of 50 eV higher than the adsorption edge.

FTIR spectra of ethylbenzene, 1-phenylethanol, acetophenone and pyridine adsorbed on the catalyst were recorded on a Nicolet 6700 FT-IR spectrometer with a resolution of 4 cm^{-1}. The catalyst sample, about 30 mg, was pressed into a self-supported wafer, pretreated at 550 °C under vacuum (<10^{-6} mbar) for 1 h, and then background spectrum was recorded after cooling the sample to 25 °C. Ethylbenzene was adsorbed on the sample at room temperature and sequentially evacuated at 450 °C and 550 °C, while 1-phneylethanol, acetophenone and pyridine were adsorbed at room temperature and sequentially evacuated at room temperature, 100 °C and 400 °C. Difference spectra were obtained by subtracting the background spectrum recorded previously.

2.3. Catalyst test

Dehydrogenation of ethylbenzene was conducted using a continuous gas-flow reactor with a fixed bed catalyst (Autoclave Engineers Ltd. Model 401 C 0286) at atmospheric pressure. In the dehydrogenation reactions, typically 0.15 g of catalyst, which had been pelletized to the particles 0.3–0.8 mm in diameter, was loaded into the reactor. The catalyst was pre-treated in a He gas flow (100 ml min^{-1}) at 550 °C for 1 h.

The reaction was started by introducing a gas mixture of ethylbenzene and He into the reactor. Ethylbenzene (0.08 ml min^{-1}; ca. 0.7 mmol min^{-1}) was fed by micro-feeder under a He flow (100 ml min^{-1}). He was used as a carrier gas instead of N_2, because N_2 can be activated to form NH_3 in the presence of H_2 over Fe catalysts. The reaction was carried out for 3 h of time-on-stream at 550 °C.

The reaction products (styrene, toluene, and benzene) and ethylbenzene were analyzed by on-line gas chromatograph equipped with FID using a HP-INNOWAX column. None of other hydrocarbons was detected. Analysis of hydrogen was performed with a TCD gas chromatograph using a packed Molecular Sieve-5A column. All the lines and valves between the cold trap and the reactor were heated to 150 °C to prevent any condensation of ethylbenzene or of the dehydrogenation products.

3. Results and Discussion

3.1. Surface area, metal composition and crystal structure of the catalysts

The specific surface areas of the catalysts are shown in Table 1. All catalysts exhibited a large surface area due to the porous structure derived from hydrotalcites as the precursors. An exceptionally small surface area of $Fe_{0.5}/Zn_3(Al_{0.5})O$ may be due to the formation of well crystallized ZnO phase arising from phase separation of $Zn(OH)_2$ from hydrotalcite during the preparation [15]. As previously reported [13], the metal compositions obtained with AA measurement well coincided with those expected from the amount of raw materials used. This is also due to the formation of hydrotalcite

precursors which can accommodate all metal components in the structure after the co-precipitation.

After calcination at 550 °C, all Mg-containing catalysts showed the X-ray reflections of MgO periclase together with $MgAl_2O_4$ spinel. MgO incorporates Ni^{2+} and Co^{2+}, as frequently reported as Mg(Ni)O and Mg(Co)O solid solutions [17,18], or Al^{3+} and Fe^{3+} as Mg(Al)O and Mg(Fe)O periclase prepared from Mg–Al and Mg–Fe hydrotalcites, respectively [19,20]. $MgAl_2O_4$ spinel also accommodates Fe^{3+} in the regular sites of $Mg(Al,Fe^{3+})_2O_4$ and Co and Ni in $Mg(Ni,Co^{2+})Al_2O_4$ or $Mg(Ni)(Al,Co^{3+})_2O_4$, depending on the valence state of Co^{2+} or Co^{3+} [21]. Mössbauer measurements suggest that much amount of Fe^{3+} was incorporated in spinel than periclase compared to the values expected from XRD analyses [13,14]. Contrarily, $Fe_{0.5}/Zn_3(Al_{0.5})O$ after drying showed reflections of $Zn(OH)_2$, indicating a separation of a part of Zn^{2+} from the Zn^{2+}–Al^{3+} hydrotalcite, resulting in the formation of ZnO as a separated phase after the calcination. $Fe_{0.5}/Zn_3(Al_{0.5})O$ showed the reflections of ZnO together with those of zinc ferrite ($ZnFe_2O_4$) [15]. This is in contrast to the results of $Fe_{0.5}/Mg_3(Al_{0.5})O$, which showed mainly Mg(Fe,Al)O periclase reflections. Mg–Fe system incorporated Fe^{3+} to form mainly Mg(Fe)O periclase, whereas Zn–Fe system formed $ZnFe_2O_4$ separately from ZnO. ZnO wurtzite forms solid solutions with Fe^{3+}, but the amount of Fe^{3+} dissolved is small [22].

3.2. Activity of Fe–Co/Mg(Al)O catalysts.

In the previous paper, we reported Fe–Co(1/1) bimetallic species as the active

sites on $Fe_{0.25}$–$Co_{0.25}/Mg_3(Al_{0.5})O$ catalyst for the dehydrogenation of ethylbenzene [13,14]. The $Fe_{0.25}$–$Co_{0.25}/Mg_3(Al_{0.5})O$ catalyst was calcined at 550, 650, 750 and 850 °C, and each was tested in the dehydrogenation of ethylbenzene (Fig. 1). In the previous paper, we reported that the activity evaluated by styrene yield at 30 min of the time-on-stream was not affected significantly by the calcination temperature [13]. In the present work, the activity was compared by the ethylbenzene conversion during the reaction after 60 min of time-on-stream. All catalysts calcined at 550, 650 and 750 °C showed almost the same conversion, but the catalyst calcined at 850 °C alone showed a decreased conversion. The selectivity to styrene was nearly the same independently of the calcination temperature between 550 and 850 °C. These results clearly indicate a decrease in the number of the active sites after the calcination at 850 °C.

XPS analyses of $Fe_{0.25}$–$Co_{0.25}/Mg_3(Al_{0.5})O$ showed peaks of Fe $2p_{3/2}$ and Fe $2p_{1/2}$ at 710.6 and 724.1 eV, respectively, which are assigned to Fe^{3+} for iron [13]. However, we could not definitely assign the valence state of Co species in $Fe_{0.25}$–$Co_{0.25}/Mg_3(Al_{0.5})O$ catalysts, because the distinction between Co^{2+} and Co^{3+} formed on the surface of the catalysts is difficult to be established by XPS [23]. In the XPS study of Re-promoted Co/Al_2O_3 catalyst [24], unusual property was observed; the Co $2p_{3/2}$ peak of the oxide shifted to a higher binding energy after reduction at 350 °C. This is most likely due to the $Co_3O_4 \rightarrow CoO$ transition, as Co^{3+} ions in the spinel structure at the lower binding energy were reduced to a +2 valence state at higher binding energy. Sexton et al. [25] reported the following peak assignment of Co $2p_{3/2}$: at 780.3 eV together with shake-up satellite at ca. 786 eV for Co^{2+}, whereas at 779.5 eV without shake-up satellite for Co^{3+}. These are in contrast to the phenomena generally

accepted, in which metal cations of the higher valence state usually have the higher binding energy than that of the lower valence state. Recently, the binding energy of Co_3O_4 was reported as Co $2p_{3/2}$ = 779.9 eV [26] or 779.6 eV together with shake-up satellite peak at 788.2 eV [27]. Actually we observed the peak of Co $2p_{3/2}$ at 780 eV together with the shake-up satellite at ca. 787 eV for $Fe_{0.25}$–$Co_{0.25}/Mg_3(Al_{0.5})O$ calcined at 550 °C (Fig. 2a). This suggests that the catalyst surface was composed of mixed valence state between Co^{3+} and Co^{2+}, possibly by the formation of isolated Co_3O_4 as fine particles.

The surface metal compositions obtained by XPS analyses are shown in Fig. 3. Co/Mg ratio was almost constant between 550 and 850 °C, whereas Fe/Mg ratio was almost constant up to 750 °C and decreased at 850 °C. The Fe/Co ratio was ca. 0.9 between 550 and 750 °C and decreased to ca. 0.4 at 850 °C. XRD observations of these catalysts showed the enhanced formation of spinel at 850 °C [13,14]. XPS observations showed an increase in the binding energy of Co $2p_{3/2}$ from 780 eV at 550 °C to 780.6 eV at 850 °C (Fig. 2b). This suggests that Co^{3+} was partly reduced to Co^{2+}; the isolated Co_3O_4 on the catalyst surface was partly converted to $(Mg,Co^{2+})(Al,Fe)_2O_4$ spinel during the calcination at increasing temperature. The ionic radii of metal components in octahedral coordination are as follows: Mg^{2+}, 0.86 Å; Al^{3+}, 0.68 Å; Fe^{3+}, 0.79 Å; Co^{2+}, 0.89 Å; Co^{3+}, 0.75 Å and Ni^{2+}, 0.83 Å [28]. It is likely that Ni^{2+} is stably incorporated not only in the hydrotalcites as precursors but also in periclase and spinel in the final $Fe_{0.25}$–$Ni_{0.25}/Mg_3(Al_{0.5})O$ (vide infra), whereas Co^{2+}/Co^{3+} incorporation in the structures is continuously accompanied by the reduction of Co^{3+} to Co^{2+} during the calcination at increasing temperature. Such reduction, or conversion of Co_3O_4 to $(Mg,Co^{2+})(Al,Fe)_2O_4$,

seems to proceed in the surface layer. This may cause an enhanced dispersion of Co species on the surface, resulting in a decrease in the Fe/Co ratio on the catalyst surface. The low activity by calcination at 850 °C (Fig. 1) is likely due to the decrease in the Fe/Co ratio, i.e., a decrease in the number of surface Fe^{3+} species as the active sites.

When the Fe–Co loading on Fe_y–$Co_y/Mg_3(Al_{0.5})O$ was varied from y = 0.1 to 0.5, the loading with y = 0.25, $Fe_{0.25}$–$Co_{0.25}/Mg_3(Al_{0.5})O$, showed a clear deactivation during 3 h of time-on-stream (Fig. 4). Decreased loading with y = 0.1, $Fe_{0.1}$–$Co_{0.1}/Mg_3(Al_{0.5})O$, showed no clear deactivation and its activity at 3 h of time-on-stream was almost the same as that of $Fe_{0.25}$–$Co_{0.25}/Mg_3(Al_{0.5})O$. Increase in the loading up to y = 0.5, $Fe_{0.5}$–$Co_{0.5}/Mg_3(Al_{0.5})O$, showed no increase in both ethylbenzene conversion and styrene selectivity compared with those on $Fe_{0.25}$–$Co_{0.25}/Mg_3(Al_{0.5})O$. The highest selectivity as well as the most sustainable styrene formation was obtained over $Fe_{0.1}$–$Co_{0.1}/Mg_3(Al_{0.5})O$ with the lowest Fe–Co(1/1) loading.

3.3. XANES and XAFS analyses of the catalysts.

The Fe *K*-edge XANES spectra of $Fe_{0.25}$–$Co_{0.25}/Mg_3(Al_{0.5})O$, $Fe_{0.25}$–$Ni_{0.25}/Mg_3(Al_{0.5})O$, $Fe_{0.5}/Mg_3(Al_{0.5})O$ and α-Fe_2O_3 are shown in Fig. 5. The energy level of Fe *K*-edge XANES spectra indicates that Fe species in the catalysts exist in the valence state of Fe^{3+} [29]. This well coincided with the results obtained by Mössabauer and XPS analyses [13,14]. The Fe *K*-edge XANES for the catalysts is a little different from that of α-Fe_2O_3 and close to that of Fe_3O_4 reported by Chen et al [29]. The pre-edge peak arises from a 1s → 3d transition, which is forbidden in

octahedral coordination but occurs in coordination without inversion center (distorted octahedral, tetrahedral) [30]. It is known from high resolution measurements that the pre-edge peak is sharp and more intensive with Fe^{3+} in tetrahedral coordination [31]. However, the pre-edge peaks of all catalysts were neither sharp nor intense and, moreover, separated into two peaks (Figs. 5Ab, c and d). Such split of the pre-edge peak of Fe^{3+} into two components were reported for α-Fe_2O_3 and $Fe(acac)_3$ [32]. In the present work, α-Fe_2O_3 (Fe^{3+} in distorted octahedral coordination) showed more intense pre-edge peak than those of all catalysts (Fig. 5Aa). Moreover, the pre-edge peak of α-Fe_2O_3 was split into two peaks, the second peak of which was substantially intensified compared to the first peak. Contrarily, all catalysts showed rather weak pre-edge peak split into two peaks, the intensities of which were almost comparable each other (Figs. 5Ab, c and d). This seems to reflect a lower distortion from the ideal octahedral symmetry with respect to all catalysts compared with that of α-Fe_2O_3.

The characteristics of the pre-edge and post-edge peaks are almost similar; the coordination symmetry around Fe^{3+} is likely to be almost the same for all catalysts, independently of the presence of Co or Ni. The shapes of pre-edge peaks (Fig. 5A) suggest that the spin states of Fe^{3+} are the same in all catalysts. Moreover, the EXAFS oscillation modes (data are not shown) are the same for all catalysts, indicating that the coordination spheres around Fe^{3+} are the same, independently of the presence of Co or Ni. The first coordination sphere around Fe^{3+} can be fitted by oxygen atom and the second sphere by aluminum atom. Thus, Fe^{3+} species is most likely distributed in the regular sites of the periclase and the spinel in the structure of the catalysts. No clear evidence of the formation of Fe–O–Co or Fe–O–Ni bonding was obtained from the

results of Fe *K*-edge XANES measurements. Relatively long wave length, i.e., low frequency, of the EXAFS oscillation also indicates a rather small contribution of heavy atom such as Fe, Co or Ni, at the neighboring sites of Fe.

The Co *K*-edge XANES spectra of $Co_{0.5}/Mg_3(Al_{0.5})O$, $Fe_{0.25}$–$Co_{0.25}/Mg_3(Al_{0.5})O$ and CoO are shown in Fig. 6. The XANES peak for CoO was observed at 7724 eV (Fig. 6a) as reported by Jacobs et al. [33] for pure CoO. It was reported that the XANES peak of Co^{3+} species was observed at 5 eV higher than that of Co^{2+} [34]. Moreover, Co_3O_4, which contains 2 atoms in 3+ oxidation state and 1 atom in 2+ oxidation state, showed the XANES peak at 3 eV higher than that of Co^{2+} [35]. Actually the energy level of the XANES peak of the catalysts was ca. 2 eV higher than that of CoO, suggesting that Co species exist as a mixed valence state between Co^{3+} and Co^{2+}, possibly as Co_3O_4, on the catalysts. This coincided with the results obtained by H_2-TPR [14] and XPS analyses, although clear assignment of the valence state of Co species was difficult in XPS (vide supra). Pre-edge features are associated with the symmetry effects in the environment of cobalt and are due to 1s → 3d transitions. As described by Moen et al. for Co *K*-edge peak [36,37], the transition is most intense when the first coordination shell lacks inversion symmetry. Therefore, the pre-edge feature is most intense for tetrahedral symmetry but should not be permitted for octahedral symmetry. In the present work, a weak pre-edge peak was observed at 7707 eV for all samples (Figs. 6a, b and c). The intensity of the pre-edge peak was higher for $Co_{0.5}/Mg_3(Al_{0.5})O$ than for $Fe_{0.25}$–$Co_{0.25}/Mg_3(Al_{0.5})O$ (Figs. 6Ab and c), suggesting that Co species in the former possess the lower symmetric state, i.e., in the more distorted octahedral coordination, than that in the latter. A shoulder observed at ca. 7717 eV for $Co_{0.5}/Mg_3(Al_{0.5})O$ (Fig.

6b) may originate from the gradual polymerization of Co^{2+} ions with oxygen ion (O^{2-}) as the concentration of Co increases in the co-preciptation solution [23]. The polymerization will finally leads to a substantial formation of isolated cobalt oxide clusters, Co_3O_4, as fine particles on the catalyst surface. This again well coincided with the results observed for $Co_{0.5}/Mg_3(Al_{0.5})O$ sample by H_2-TPR and XRD [14].

$Fe_{0.25}$–$Co_{0.25}/Mg_3(Al_{0.5})O$ showed a slightly different mode in the EXAFS oscillation from that of $Co_{0.5}/Mg_3(Al_{0.5})O$ (data are not shown) and, further, showed the stronger peak in the second coordination sphere than $Co_{0.5}/Mg_3(Al_{0.5})O$ in Fourier transforms of EXAFS oscillation (Figs. 7f and g). These suggest that the coordination sphere around Co species differ each other between in $Fe_{0.25}$–$Co_{0.25}/Mg_3(Al_{0.5})O$ and $Co_{0.5}/Mg_3(Al_{0.5})O$. The peak intensity in the second coordination sphere frequently varies due to the following reasons: 1) several atoms coordinate to Co changing the bond distance, or 2) heavy atoms coordinate to Co, e.g., by forming Co–O–Fe or Co–O–Co bonding. Moreover, the peak position varied and the peak intensity was weaker at the first coordination sphere (Co–O bonding) (Figs. 7f and g) than those observed for Fe species (Fe–O bonding) (Figs. 7b, c and d), indicating that Co–O bond length was not constant. Neither Co nor Ni species was found around Fe species as observed for Fe *K*-edge XANES and EXAFS oscillation. Compared with such simple coordination sphere around Fe, the coordination sphere around Co species was more complex, suggesting that Co–O–Co and Co–O–Fe bonding were contaminated. This may coincide with the formation of Co_3O_4 as well as the results obtained in the previous paper; Co species tends to be isolated from the periclase and spinel structures to form CoO_x in Co-rich catalysts [14].

The energy levels of Ni *K*-edge XANES spectra of $Fe_{0.25}$–$Ni_{0.25}/Mg_3(Al_{0.5})O$, $Ni_{0.5}/Mg_3(Al_{0.5})O$ and NiO (Fig. 8) indicate that Ni species in the catalysts is in the valence state of Ni^{2+}. The Ni *K*-edge XANES for the calcined catalyst is very similar to that of NiO, with the rock salt structure, i.e., Ni cations basically octahedrally coordinated by oxygen atoms. The characteristics of pre-edge (Fig. 8A) and post-edge suggest that the coordination symmetry around Ni^{2+} is slightly distorted octahedral [26], independently of the copresence of Fe. EXAFS oscillation of $Ni_{0.5}/Mg_3(Al_{0.5})O$ differs from that of $Fe_{0.25}$–$Ni_{0.25}/Mg_3(Al_{0.5})O$, and shows a short wave length, suggesting the formation of Ni–O–Ni bonding. Actually the spectrum can be fitted with oxygen in the first coordination sphere and with Ni in the second coordination sphere. In the presence of Fe, i.e., $Fe_{0.25}$–$Ni_{0.25}/Mg_3(Al_{0.5})O$, the oscillation with the short wave length almost disappeared and the peak of the second coordination sphere was weakened in Fourier transforms of EXAFS oscillation, suggesting that Ni–O–Ni contribution was lowered or that Ni–O–Fe contribution was almost negligible (Figs. 7i and j).

All these data suggest that each Fe, Co and Ni was mainly coordinated by Al (or Mg) through oxygen atom except Co–O–Fe and Co–O–Co bonding possibly on the surface of $Mg_3Fe_{0.25}Co_{0.25}Al_{0.5}$ catalyst particles.

3.4. FTIR of ethylbenzene adsorbed on the catalysts

The FTIR spectra of ethylbenzene adsorbed on $Fe_{0.5}/Mg_3(Al_{0.5})O$, $Fe_{0.25}$–$Co_{0.25}/Mg_3(Al_{0.5})O$ and $Fe_{0.5}/Zn_3(Al_{0,5})O$ catalysts are shown in Figs. 9a-f. At 450 ºC, $Fe_{0.5}/Zn_3(Al_{0.5})O$ showed broad absorption bands around 1360 and 1560 cm^{-1}

corresponded to hydrocarbons decomposition fragments, presumably as oligomers of reactant and/or product species (Fig. 9e) [38,39]. It was also reported that intense IR bands were observed at about 1360 and 1590 cm^{-1} for ground graphite, carbon blacks and some activated carbons [40]. However, these bands totally disappeared at 550 ºC, suggesting that these fragments were almost decomposed and desorbed, leading to no coke formation on the catalysts, (Fig. 9f). $Fe_{0.5}/Zn_3(Al_{0.5})O$ showed also weak absorption bands at 1445, 1494 and 1602 cm^{-1} (Fig. 9e) at 450 ºC, which are all assigned to ν(C–C) of aromatic ring of ethylbenzene [41], suggesting a weak adsorption of ethylbenzne via its aromatic ring on $Fe_{0.5}/Zn_3(Al_{0.5})O$. These indicate that ethylbenzene was adsorbed on $Fe_{0.5}/Zn_3(Al_{0.5})O$, but followed by decomposition, leading to no substantial formation of styrene.

Although the broad bands around 1360 and 1560 cm^{-1} were observed on $Fe_{0.25}$–$Co_{0.25}/Mg_3(Al_{0.5})O$ at 450 and 550 ºC, they are not intensive as those on $Fe_{0.5}/Zn_3(Al_{0.5})O$ (Figs. 9c and d). On $Fe_{0.25}$–$Co_{0.25}/Mg_3(Al_{0.5})O$ at 450 and 550 ºC (Figs. 9c and d), the absorption bands of ν(C–C) of aromatic ring of ethylbenzene were observed at 1445, 1481, 1494 and 1602 cm^{-1} together with the band of ν(C–H) of aromatic ring of ethylbenzene at 1385 cm^{-1} [41]. Among these bands, the ν(C–C) band at 1481 cm^{-1} was most intensified at 550 ºC. The wave numbers of these bands well coincided with those observed for ethylbenzene adsorbed on β-zeolite [41]. For ethylbenzene in gas phase, the ν(C–C) bands were observed at 1460 and 1498 cm^{-1}, whereas the ν(C–H) band was observed at 1382 cm^{-1} [41]. Compared with these values in gas phase, the ν(C–C) bands were shifted toward lower wave numbers (from 1460 and 1498 cm^{-1} to 1445, 1481 and 1494 cm^{-1}), whereas the ν(C–H) band showed no

significant shift (1385 cm^{-1}), on the catalyst. When benzene was adsorbed on α-Fe_2O_3, a strong absorption band appeared at 1481 cm^{-1} assigned to ν_{19} vibration [42] composed by out-of plane deformation vibrations. This indicates that there is an interaction with an electron-withdrawing center nearly perpendicular to the aromatic ring [43]. It is most likely that ethylbenzene was strongly adsorbed on $Fe_{0.25}$–$Co_{0.25}/Mg_3(Al_{0.5})O$ through the aromatic ring, presumably via a π-type bonding interaction with rather strong Lewis acidic centers. On the other hand, $Fe_{0.5}/Mg_3(Al_{0.5})O$ showed no absorption band between 1368 and 1602 cm^{-1}, i.e., all bands of ν(C–C) at 1445, 1481, 1494 and 1605 cm^{-1} and of ν(C–H) at 1385 cm^{-1} of aromatic ring of ethylbenzene adsorbed were not observed on $Fe_{0.5}/Mg_3(Al_{0.5})O$ even under high magnification (Figs. 9a and b). This suggests that π-type bonding interaction of aromatic ring with Lewis acid centers was not strong on $Fe_{0.5}/Mg_3(Al_{0.5})O$ as on $Fe_{0.25}$–$Co_{0.25}/Mg_3(Al_{0.5})O$, although $Fe_5/Mg_3(Al_{0.5})O$ possesses Lewis acid sites on the surface (vide infra).

$Fe_{0.25}$–$Co_{0.25}/Mg_3(Al_{0.5})O$ showed further the absorption bands at 1095, 1153, 1198, 1246 and 1307 cm^{-1} at 450 and 550 ºC (Figs. 9c and d). The most intense band at 1246 cm^{-1} may be assigned to C–O stretching vibration, because the absorption band of C–O bond was observed at 1211 cm^{-1} for 1-butanol adsorbed on Pt electrode [44]. The weak band at 1095 cm^{-1} is assigned to coke formed on the catalyst surface as observed in benzene alkylation with propylene over Hβ-zeolite [45]. The broad band at 1307 cm^{-1} may be assigned to vinyl C–H bending mode of styrene formed from ethylbenzene and the weak band at 1198 cm^{-1} is assigned to styrene in gaseous phase [38]. These suggest that styrene was formed by the dehydrogenation during the FTIR measurements of ethylbenzene adsorption. Similar pattern of the absorption bands was observed on

$Fe_{0.5}/Mg_3(Al_{0.5})O$, although not intensive as on $Fe_{0.25}$–$Co_{0.25}/Mg_3(Al_{0.5})O$. The band at 1246 cm^{-1} clearly indicated the C–O bonding also on $Fe_{0.5}/Mg_3(Al_{0.5})O$. Moreover, a new band appeared at 1676 cm^{-1} at 500 ºC (Fig. 9b) and may be assigned to free CH_2=CH_2 [45], suggesting that an occurring of styrene decomposition on $Mg_3Fe_{0.5}Al_{0.5}$.

3.5. FTIR of pyridine adsorbed on the catalysts

The basicity of the $Fe_{0.5}/Mg_{3-x}Zn_x(Al_{0.5})O$ catalysts was evaluated by the CO_2–TPD and FTIR of CO_2 adsorbed on the catalysts, and the important role of Mg^{2+}–O^{2-} basic site on the activity was suggested in the previous paper [15]. According to the results of FTIR measurements of ethylbenzene adsorbed on the catalysts, the adsorption of aromatic ring of ethylbenzene on the Lewis acid sites was suggested as an intermediate during dehydrogenation (Fig. 9). The nature of the Lewis acid sites is likely different each other on $Fe_{0.5}/Mg_3(Al_{0.5})O$ and $Fe_{0.25}$–$Co_{0.25}/Mg_3(Al_{0.5})O$. The surface acidity was evaluated by the FTIR of pyridine adsorbed on the catalysts. When pyridine was adsorbed at room temperature and sequentially evacuated at 100 °C, both $Fe_{0.25}$–$Co_{0.25}/Mg_3(Al_{0.5})O$ (Fig. 10a) and $Fe_{0.5}/Mg_3(Al_{0.5})O$ (Fig.10c) showed similar pattern of the spectra. The bands at 1602, 1575 and 1443 cm^{-1} can be ascribed to stretching modes of the pyridine ring coordinated to surface Lewis acid sites, i.e. coordinatively unsaturated Fe^{3+} species (L-py) [46], while the band at 1488 cm^{-1} contains contributions due to vibration of both pyridinium ions adsorbed on Brønsted acid sites (B-Py) and coordinatively adsorbed pyridine molecules (L-Py) [47]. The latter band at 1488 cm^{-1} was more intense on $Fe_{0.5}/Mg_3(Al_{0.5})O$ than on

$Fe_{0.25}$–$Co_{0.25}/Mg_3(Al_{0.5})O$. The band at 1543 cm^{-1} was observed only on $Fe_{0.5}/Mg_3(Al_{0.5})O$ and is assigned to vibrations of pyridine molecules adsorbed on Brønsted acid sites (B-Py) [47]. Both bands at 1560 and 1507 cm^{-1} can not be assigned to any species and were more intensely observed on $Mg_3Fe_{0.5}Al_{0.5}$ than on $Fe_{0.25}$–$Co_{0.25}/Mg_3(Al_{0.5})O$. These results indicate that Lewis acid sites exist on both $Fe_{0.5}/Mg_3(Al_{0.5})O$ and $Fe_{0.25}$–$Co_{0.25}/Mg_3(Al_{0.5})O$ surface together with small amounts of Brønsted acid sites, the latter, however, were more enhanced on $Fe_{0.5}/Mg_3(Al_{0.5})O$ than on $Fe_{0.25}$–$Co_{0.25}/Mg_3(Al_{0.5})O$.

When pyridine was evacuated at 400 °C on $Fe_{0.25}$–$Co_{0.25}/Mg_3(Al_{0.5})O$ (Fig. 10b), the band at 1443 cm^{-1} was substantially weakened, the bands at 1602 and 1575 cm^{-1} disappeared, and a new band at 1616 cm^{-1} ascribed to L-Py appeared [48]. This indicates that the nature of Lewis acid sites was changed at 400 °C on $Fe_{0.25}$–$Co_{0.25}/Mg_3(Al_{0.5})O$. On the other hand, on $Fe_{0.5}/Mg_3(Al_{0.5})O$ after evacuation at 400 °C (Fig. 10d), all bands of L-Py were proportionately weakened except that the band at 1488 cm^{-1} of B-Py almost disappeared, suggesting that the Brønsted acid sites were converted to the Lewis acid sites at 400 °C on $Fe_{0.5}/Mg_3(Al_{0.5})O$.

When pyridine was evacuated at 100 ºC on $Fe_{0.5}/Zn_3(Al_{0.5})O$, only weak bands at 1443 and 1592 cm^{-1} were observed (Fig. 10e). The band at 1443 cm^{-1} is assigned to L-Py, whereas the band at 1592 cm^{-1} is assigned to physisorbed or hydrogen-bonded pyridine (H-Py) [48]. These bands almost disappeared after evacuation at 400 ºC (Fig. 10f), indicating that no significant acid site was formed on $Fe_{0.5}/Zn_3(Al_{0.5})O$.

It is concluded that both $Fe_{0.25}$–$Co_{0.25}/Mg_3(Al_{0.5})O$ and $Fe_{0.5}/Mg_3(Al_{0.5})O$ possess Lewis acid sites, whereas $Fe_{0.5}/Zn_3(Al_{0.5})O$ does not. The Lewis acid sites may be

originated from Fe^{3+} species on the catalyst surface and the nature is different each other between $Fe_{0.25}$–$Co_{0.25}/Mg_3(Al_{0.5})O$ and $Fe_{0.5}/Mg_3(Al_{0.5})O$. Judging from the results of TPR measurements, i.e., Fe^{3+} was reduced at lower temperature on $Fe_{0.25}$–$Co_{0.25}/Mg_3(Al_{0.5})O$ than on $Fe_{0.5}/Mg_3(Al_{0.5})O$ [13,14], the Fe^{3+} species seems more reactive on $Fe_{0.25}$–$Co_{0.25}/Mg_3(Al_{0.5})O$ than on $Fe_{0.5}/Mg_3(Al_{0.5})O$.

3.6. Catalytic mechanism.

In ethylbenzene dehydrogenation over a commercial Fe_2O_3 catalyst, Măicăneanu et al. [49] proposed a mixed acid–basic and reduction–oxidation mechanism based on the kinetic study; a formation of π-adsorbed intermediate on Fe^{3+} acid centers, followed by elimination of two hydrogen ions from two C–H ethylic groups on basic centers with electrons transfer to Fe^{3+} to form styrene and H_2. Miura et al. [50] proposed an initiation by the α-H^+ abstraction on the basic site, followed by the formation of π-adsorbed intermediate on Fe^{3+} acid centers, based on H-D exchange study using the same catalyst. In the previous paper [15], we proposed the following mechanism: ethylbenzene (EB) was H^+ abstracted on Mg^{2+}–O^{2-} basic sites, followed by further dehydrogenation to styrene (St) via the reduction of Fe^{3+} to Fe^{2+} (1). Both St and H_2 were simultaneously

$$2Mg^{2+}O^{2-}Fe^{3+} + EB_{ad} \rightarrow 2Mg^{2+}OH^{-}Fe^{2+} + St_{ad} \quad (1)$$

desorbed with the reoxidation of Fe^{2+} to Fe^{3+} (2). Recently, Oliveira et al. [51] reported

$$2Mg^{2+}OH^{-}Fe^{2+} + St_{ad} \rightarrow 2Mg^{2+}O^{2-}Fe^{3+} + St + H_2 \quad (2)$$

that, in ethylbenzene dehydrogenation over Fe/MCM-41 catalyst, the Fe^{3+} acid site of the catalyst adsorbs ethylbenzene, reversibly abstracting the α-hydrogen at a basic OH

adjacent to the acid site, whereas the O^- base sites abstracts the β-hydrogen. A similar mechanism was also reported in the oxidative dehydrogenation of ethylbenzene on the Si–Al catalysts; the acid site adsorbs ethylbenzene, reversibly abstracting the α-hydrogen at the basic OH adjacent to the acid site, and the base site activates gaseous oxygen to form O^- which abstracts the β-hydrogen leading to styrene formation [52].

In the present work, we presumably assigned the band at 1246 cm^{-1} to ν(C–O). This assignment may be confirmed by the FTIR measurements of 1-phenylethanol and acetophenone as a reference. When 1-phneylethanol (Fig. 9g) was adsorbed on $Mg_3Fe_{0.25}Co_{0.25}Al_{0.5}$ at room temperature, two absorption bands appeared at 1207 and 1262 cm^{-1} together with those at 1368, 1445, 1494 and 1602 cm^{-1}. Acetophenone (Fig. 9h) showed also similar patterns of absorption, i.e., two bands at 1216 and 1262 cm^{-1} together with those at 1368, 1445, 1494 and 1602 cm^{-1}. The latter four bands were also observed at 100 ºC (Figs. 9h and j) and can be assigned to ν(C–C) of aromatic ring of 1-phenylethanol and acetophenone strongly adsorbed on Lewis acid sites as observed for ethylbenzene adsorbed on $Mg_3Fe_{0.25}Co_{0.25}Al_{0.5}$ (Figs. 9c and d). The former two bands can be assigned to two types of ν(C–O) of ethyl α-C bound to Mg^{2+} through oxygen, one of which (1262 cm^{-1}) shifted to 1282 cm^{-1} at 100 ºC for 1-phenylethanol (Fig. 9h). In both 1-phenylethanol and acetophenone, two types of C–O bond may be formed when adsorbed on $Mg_3Fe_{0.25}Co_{0.25}Al_{0.5}$, and a small shift is expected dependently of the presence or absence of H (Scheme 1). The band around 1680 cm^{-1} may be assigned to ν(C=O) of free acetophenone (Fig. 9i), or that formed from 1-phenylethanol on the catalyst (Fig. 9g) [53]. The band of ν(C=O) of acetophenone shifted toward lower wave numbers at 100 ºC (Figs. 9h and j).

It is thus most likely that the band at 1246 cm^{-1} observed for ethylbenzene on both $Mg_3Fe_{0.25}Co_{0.25}Al_{0.5}$ and $Mg_3Fe_{0.5}Al_{0.5}$ (Figs. 9a-d) is assigned to ν(C–O) of ethyl α-C bound to Mg^{2+} through oxygen. The surface base sites generated on O^{2-} bound to Mg^{2+} near Fe^{3+} sites are responsible for H^+-abstraction, and further the dehydrogenation reaction was accelerated by the reduction-oxidation between Fe^{3+} and Fe^{2+} [13-15]. The dehydrogenation mechanism is proposed as shown in Scheme 2. Ethylbenzene was strongly adsorbed on $Fe_{0.25}$–$Co_{0.25}/Mg_3(Al_{0.5})O$, whereas weakly on $Fe_{0.5}/Mg_3(Al_{0.5})O$, through the aromatic ring, via a π-type bonding interaction with Fe^{3+} Lewis acid sites. Simultaneously, α-H^+ abstraction took place on O^{2-} basic sites bound to Mg^{2+} (intermediate I) as proposed in ethylbenzene dehydrogenation by Miura et al. [50] and Tagawa et al. [52]. This may be followed by the bond formation between $O^{2-}(–Mg^{2+})$ and α-C of ethylbenzene; the strong π-adsorption of ethylbenzene makes ethyl α-C electron deficient and reactive with O^{2-}. Nucleophilic attack of basic oxygen to carbon atoms is frequently observed in organic synthesis. Ethylbenzene was α-H^+ abstracted through intermediate I to form intermediate II on $Mg^{2+}O^{2-}$ basic sites, which was further dehydrogenated to styrene via the reduction of Fe^{3+} to Fe^{2+}. The intermediate II just before dehydrogenation was stabilized by mesomeric effect caused by the presence of $H^{\delta-}$, which then reacted with β-H^+ of ethyl group to form H_2. Both styrene and H_2 were desorbed simultaneously with the reoxidation of Fe^{2+} to Fe^{3+}, and this step seems to be a rate determining step of this dehydrogenation reaction. Actually trace amount of styrene was detected in gas phase (1198 cm^{-1}) during the FTIR measurements of ethylbenzene adsorbed on $Fe_{0.5}/Mg_3(Al_{0.5})O$ and $Fe_{0.25}$–$Co_{0.25}/Mg_3(Al_{0.5})O$ catalysts (Figs. 9b and d). Such acid-base catalyzed and reduction-oxidation assisted reaction accelerates catalytic

cycle for ethylbenzene dehydrogenation. The addition of Co resulted in the formation of $Co^{3+/2+}$ species on the catalyst surface and enhanced the reactivity of Fe^{3+} species as the Lewis acid sites by withdrawing electron through a Fe^{3+}–O–$Co^{3+/2+}$ bond. This leads to the enhanced formation of C–O bond and further the enhanced reduction-oxidation of $Fe^{3+/2+}$ species, resulting in an enhanced activity of $Fe_{0.25}$–$Co_{0.25}/Mg_3(Al_{0.5})O$ catalyst in the dehydrogenation of ethylbenzene.

4. Conclusion

Fe–Co/Mg(Al)O catalysts derived from hydrotalcite showed a synergetic increase in the activity by Fe-Co bimetal formation. Co species exists as a mixture of Co^{3+}/Co^{2+} together with Fe^{3+}, although Co^{2+} nitrate was used as a raw material in the catalyst preparation. Co addition enhanced Lewis acidity of the Fe^{3+} acid sites by forming Fe^{3+}–O–$Co^{3+/2+}$(1/1) bimetallic species, leading to an enhanced π-bonding of aromatic ring of ethylbenzene to the Fe^{3+}. Thus activated ethyl group of ethylbenzene adsorbed on the Fe^{3+} Lewis acid sites was α-H^+ abstracted on Mg^{2+}–O^{2-} basic sites, to form C–O bond on the catalyst surface. The α-H^+ abstraction by O^{2-}(–Mg^{2+}) might proceed via C–O–Mg bonding intermediate, followed by β-H^+ abstraction, leading to the formations of styrene and H_2. It is concluded that the mixed catalytic mechanism by the Fe^{3+} Lewis acid–O^{2-}(–Mg^{2+}) base couple and the Fe^{3+}/Fe^{2+} reduction-oxidation cycle was effectively assisted by Co^{3+}/Co^{2+} couple, leading to a good catalytic activity for the dehydrogenation of ethylbenzene.

Acknowledgements

This publication was based on work supported by Award No. K-C1-019-12 made by King Abdullah University of Science and Technology (KAUST). The support of King Fahd University of Petroleum and Minerals (KFUPM) is also highly appreciated. The XAFS measurements at the SPring-8 were carried out by the approval (proposal No. 2010B1184) of Japan Synchrotron Radiation Research Institute (JASRI). The authors also acknowledge Japan Cooperation Center, Petroleum (JCCP) for giving the opportunity of this collaborative research.

References

1. E.H. Lee, Catal. Rev. Eng. Sci. 8 (1973) 285–305.
2. A.A. Savoretti, D.O. Borio, V. Bucalá, J.A. Porras, Chem. Eng. Sci. 54 (1999) 205–213.
3. M. Muhler, J. Schütze, M. Wesemann, T. Rayment, A. Dent, R. Schlögl, G. Ertl, J. Catal. 126 (1990) 339–360.
4. J. Matsui, T. Sodesawa, F. Nozaki, Appl. Catal. 67 (1991) 179–188.
5. N. Mimura, M. Saito, Catal. Today 55 (2000) 173–178.
6. B.D. Herzog, H.F. Raso, Ind. Eng. Chem. Prod. Res. Dev. 23 (1984) 187–196.
7. M. Muhler, R. Schlögl, A. Reller, G. Ertl, Catal. Lett. 2 (1989) 201–210.
8. I. Rossetti, E. Bencini, L. Trentini, L. Forni, Appl. Catal. A: Gen. 292 (2005) 118–123.
9. M. Baghalha, O. Ebrahimpour, Appl. Catal. A: Gen. 326 (2007) 143–151.
10. A.C. Oliveira, J.L.G. Fierro, A. Valentini, P.S.S. Nobre, M. do Carmo Rangel, Catal. Today 85 (2003) 49–57.
11. D.E. Stobbe, F.R. van Buren, A.W. Stobbe-Kreemers, A.J. van Dillen, J.W. Geus, J. Chem. Soc., Faraday Trans. 87 (1991) 1631–1637.
12. Y. Ohishi, T. Kawabata, T. Shishido, K. Takaki, Q. Zhang, Y. Wang, K. Nomura, K. Takehira, Appl. Catal. A Gen. 288 (2005) 220–231.
13. R.J. Balasamy, A. Khurshid, A.A.S. Al-Ali, L.A. Atanda, K. Sagata, M. Asamoto, H. Yahiro, K. Nomura, T. Sano, K. Takehira, S.S. Al-Khattaf, Appl. Catal. A Gen. 390 (2010) 225–234.

14. L.A. Atanda, R.J. Balasamy, A. Khurshid, A.A.S. Al-Ali, K. Sagata, M. Asamoto, H. Yahiro, K. Nomura, T. Sano, K. Takehira, S.S. Al-Khattaf, Appl. Catal. A Gen. 396 (2011) 107–115.
15. R.J. Balasamy, B.B. Tope, A. Khurshid, A.A.S. Al-Ali, L.A. Atanda, K. Sagata, M. Asamoto, H. Yahiro, K. Nomura, T. Sano, K. Takehira, S.S. Al-Khattaf, Appl. Catal. A Gen. 398 (2011) 113–122.
16. T. Taguchi, T. Ozawa, H. Yashiro, Phys. Scr. T115 (2005) 205–206.
17. D. Li, I. Atake, T. Shishido, Y. Oumi, T. Sano, K. Takehira, J. Catal. 250 (2007) 299–312.
18. C.A. Querini, M.A. Ulla, F. Requejo, J. Soria, U.A. Sedrán, E.E. Miró, Appl. Catal. B Environ. 15 (1998) 5–19.
19. F. Cavani, F. Trifiro, A. Vaccari, Catal. Today 11 (1991) 173–301.
20. O.P. Ferreira, O.L. Alves, D.X. Gouveia, A.G. Souza Filho, J.A.C. de Paiva, J.M. Filho, J. Solid State Chem. 177 (2004) 3058–3069.
21. Z. Jiang, J. Yu, J. Cheng, T. Xiao, M.O. Jones, Z. Hao, P.P. Edwards, Fuel Process. Technol. 91 (2010) 97–102.
22. G.Y. Ahn, S.-I. Park, I.-B. Shim, C.S. Kim, J. Magn. Magn. Mater. 282 (2004) 166–169.
23. J.-H. Park, C.H. Park, I.-S. Nam, Appl. Catal. A Gen. 277 (2004) 271–279.
24. G. Jacobs, J.A. Chaney, P.M. Patterson, T.K. Dasa, B.H. Davis, Appl. Catal. A Gen. 264 (2004) 203–212.
25. B.A. Sexton, A.E. Hughes, T.W. Turney, J. Catal. 97 (1986) 390–406.
26. F. Morales, F.M.F. de Groot, O.L.J. Gijzeman, A. Mens, O. Stephan, B.M.

Weckhuysen, J. Catal. 230 (2005) 301–308.

27. J.E. Herrera, D.E. Resasco, J. Catal. 221 (2004) 354–364.

28. R.D Shannon, Acta Crystallogr. A32 (1976) 751–767.

29. Z. Yu, D. Chen, M. Rønning, T. Vrålstad, E. Ochoa-Fernández, A. Holmen, Appl. Catal. A Gen. 338 (2008) 136–146.

30. F. Heinrich, C. Schmidt, E. Löffler, M. Menzel, W. Grünert, J. Catal. 212 (2002) 157–172.

31. G. Calas, J. Petiau, Solid State Commun. 48 (1983) 625–629.

32. G. Berlier, G. Spoto, P. Fisicaro, A. Zecchina, E. Giamello, C. Lamberti, Microchem. J. 71 (2002) 101–116.

33. G. Jacobs, J.A. Chaney, P.M. Patterson, T.K. Das, B.H. Davis, Appl. Catal. A Gen. 264 (2004) 203–212.

34. M. Mhamdi, S. Khaddar-Zine, A. Ghorbel, Appl. Catal. A Gen. 337 (2008) 39–47.

35. G. Jacobs, T.K. Das, P.M. Patterson, J. Li, L. Sanchez, B.H. Davis, Appl. Catal. A Gen. 247 (2003) 335–343.

36. A. Moen, D.G. Nicholson, M. Ronning, G.M. Lamble, J.-F. Lee, H. Emerich, J. Chem. Soc., Faraday Trans. 93 (1997) 4071–4077.

37. A. Moen, D.G. Nicholson, B.S. Clausen, P.L. Hansen, A. Molenbroek, G. Steffensen, Chem. Mater. 9 (1997) 1241-1247.

38. W.P. Addiego, C.A. Estrada, D.W. Goodman, M.P. Rosynek, R.G. Windham, J. Catal. 146 (1994) 407–414.

39. A.K. Ghosh, R.A. Kydd, J. Catal. 100 (1986) 185–195.

40. R.A. Friedel, G.L. Carlson, Fuel 51 (1972) 194–198.

41. Y. Du, H. Wang, S. Chen, J. Mol. Catal. A Chem. 179 (2002) 253–261.

42. P.C. Painter, J.L. Koenig, Specrrochim. Acta A 33, 1003 (1977) 1019–1024.

43. G. Busca, T. Zerlia, V. Lorenzelli, A. Girelli, J. Catal. 88 (1984) 131–136.

44. N.-H. Li, S.-G. Sun, J. Electroanal. Chem. 436 (1997) 65-72.

45. M. Han, S. Lin, E. Roduner, Appl. Catal. A Gen. 243 (2003) 175–184.

46. G. Neri, G. Rizzo, S. Galvagno, G. Loiacono, A. Donato, M.G. Musolino, R. Pietropaolo, E. Rombi, Appl. Catal. A Gen. 274 (2004) 243–251.

47. B.H. Davis, R.A. Keogh, S. Alerasool, D.J. Zalewski, D.E. Day, P.K. Doolin, J. Catal. 183 (1999) 45–52.

48. G. Connel, J.A. Dumesic, J. Catal. 101 (1986) 103–113 (1986).

49. N. Dulamiţă, A. Măicăneanu, D.C. Sayle, M. Stanca, R. Crăciun, M. Olea, C. Afloroaei, A. Fodor, Appl. Catal. A: Gen. 287 (2005) 9–18.

50. H. Miura, R. Ansai, H. Kawai, React. Kinet. Catal. Lett. 53 (1994) 323–329.

51. A.H. de Morais Batista, F.F. de Sousa, S.B. Honorato, A.P. Ayala, J.M. Filho, F.W. de Sousa, A.N. Pinheiro, J.C.S. de Araujo, R.F. Nascimento, A. Valentini, A.C. Oliveira, J. Mol. Catal. A Chem. 315 (2010) 86–98.

52. T. Tagawa, T. Hattori, Y. Murakami, J. Catal. 75 (1982) 66-77.

53. R.V. Malyala, C.V. Rode, M. Arai, S.G. Hegde, R.V. Chaudhari, Appl. Catal. A Gen. 193 (2000) 71–86.

Table 1. Specific surface area of the catalysts.[a)]

Catalyst	Specific surface area / $m^2\ g_{cat}^{-1}$
$Fe_{0.5}/Mg_3(Al_{0.5})O$	178
$Fe_{0.25}$–$Co_{0.25}/Mg_3(Al_{0.5})O$	187
$Fe_{0.1}$–$Co_{0.1}/Mg_3(Al_{0.5})O$	198
$Fe_{0.5}$–$Co_{0.5}/Mg_3(Al_{0.5})O$	175
$Co_{0.5}/Mg_3(Al_{0.5})O$	171
$Fe_{0.25}$–$Ni_{0.25}/Mg_3(Al_{0.5})O$	238
$Ni_{0.5}/Mg_3(Al_{0.5})O$	181
$Fe_{0.5}/Zn_3(Al_{0.5})O$	109

a) The catalysts were prepared by co-precipitation of metal nitrates at pH = 10.0 and calcined at 550 °C for 12 h.

Figure captions

Figure 1. Ethylbenzene dehydrogenation over $Fe_{0.25}$–$Co_{0.25}/Mg_3(Al_{0.5})O$ catalysts calcined at 550, 650, 750 and 850 °C.

Reaction temperature, 550 °C ; catalyst, 0.15 g; ethylbenzene, 0.08 ml min^{-1}(ca. 0.7 mmol min^{-1}); He, 100 ml min^{-1}.

Full line, ethylbenzene conversion; dotted line, styrene selectivity.

●, $Fe_{0.25}$–$Co_{0.25}/Mg_3(Al_{0.5})O$ (550); ■, $Fe_{0.25}$–$Co_{0.25}/Mg_3(Al_{0.5})O$ (650); ▲, $Fe_{0.25}$–$Co_{0.25}/Mg_3(Al_{0.5})O$ (750); ○, $Fe_{0.25}$–$Co_{0.25}/Mg_3(Al_{0.5})O$ (850).

Figure 2. Co 2p XP spectrum $Fe_{0.25}$–$Co_{0.25}/Mg_3(Al_{0.5})O$ catalysts.

a) calcined at 550 °C; b) calcined at 850 °C.

Figure 3. Surface metal composition of $Fe_{0.25}$–$Co_{0.25}/Mg_3(Al_{0.5})O$ catalysts calcined at 550, 650, 750 and 850 °C.

The metal composition was calculated from the XPS analytical results.

●, Fe/Mg ratio; ■, Co/Mg ratio.

Figure 4. Ethylbenzene dehydrogenation over Fe_x–$Co_x/Mg_3(Al_{0.5})O$ (x = 0.1, 0.25 and 0.5) catalysts calcined at 550 °C.

Reaction temperature, 550 °C ; catalyst, 0.15 g; ethylbenzene, 0.08 ml min^{-1}(ca. 0.7 mmol min^{-1}); He, 100 ml min^{-1}.

Full line, ethylbenzene conversion; dotted line, styrene selectivity.

■, $Fe_{0.1}$–$Co_{0.1}/Mg_3(Al_{0.5})O$; ●, $Fe_{0.25}$–$Co_{0.25}/Mg_3(Al_{0.5})O$; ▲, $Fe_{0.5}$–$Co_{0.5}/Mg_3(Al_{0.5})O$.

Figure 5. Fe *K*-edge XANES and the pre-edge spectra (A) of $Fe_{0.5}/Mg_3(Al_{0.5})O$,

$Fe_{0.25}$–$Co_{0.25}/Mg_3(Al_{0.5})O$ and $Fe_{0.25}$–$Ni_{0.25}/Mg_3(Al_{0.5})O$ catalysts with standard material.

(a) α-Fe_2O_3; (b) $Fe_{0.5}/Mg_3(Al_{0.5})O$; (c) $Fe_{0.25}$–$Co_{0.25}/Mg_3(Al_{0.5})O$; (d) $Fe_{0.25}$–$Ni_{0.25}/Mg_3(Al_{0.5})O$.

Figure 6. Co *K*–edge XANES and the pre–edge spectra (A) of $Co_{0.5}/Mg_3(Al_{0.5})O$ and $Fe_{0.25}$–$Co_{0.25}/Mg_3(Al_{0.5})O$ catalysts with standard material.

(a) CoO; (b) $Co_{0.5}/Mg_3(Al_{0.5})O$; (c) $Fe_{0.25}$–$Co_{0.25}/Mg_3(Al_{0.5})O$.

Figure 7. Fourier transformed Fe, Co and Ni EXAFS data of the catalysts with standard materials.

Fe: (a) α-Fe_2O_3; (b) $Fe_{0.5}/Mg_3(Al_{0.5})O$; (c) $Fe_{0.25}$–$Co_{0.25}/Mg_3(Al_{0.5})O$; (d) $Fe_{0.25}$–$Ni_{0.25}/Mg_3(Al_{0.5})O$.

Co: (e) CoO; (f) $Co_{0.5}/Mg_3(Al_{0.5})O$; (g) $Fe_{0.25}$–$Co_{0.25}/Mg_3(Al_{0.5})O$.

Ni: (h) NiO; (i) $Ni_{0.5}/Mg_3(Al_{0.5})O$; (j) $Fe_{0.25}$–$Ni_{0.25}/Mg_3(Al_{0.5})O$.

Figure 8. Ni *K*–edge XANES and the pre–edge spectra (A) of $Ni_{0.5}/Mg_3(Al_{0.5})O$ and $Fe_{0.25}$–$Ni_{0.25}/Mg_3(Al_{0.5})O$ catalysts with standard material.

(a) NiO; (b) $Ni_{0.5}/Mg_3(Al_{0.5})O$; (c) $Fe_{0.25}$–$Ni_{0.25}/Mg_3(Al_{0.5})O$.

Figure 9. FTIR spectra of ethylbenzene and 1-phenylethanol adsorbed on $Fe_{0.5}/Mg_3(Al_{0.5})O$, $Fe_{0.25}$–$Co_{0.25}/Mg_3(Al_{0.5})O$ and $Fe_{0.5}/Zn_3(Al_{0.5})O$ catalysts.

Ethylbenzene: (a) $Fe_{0.5}/Mg_3(Al_{0.5})O$, 450 ^oC; (b) $Fe_{0.5}/Mg_3(Al_{0.5})O$, 550 ^oC; (c) $Fe_{0.25}$–$Co_{0.25}/Mg_3(Al_{0.5})O$, 450 ^oC; (d) $Fe_{0.25}$–$Co_{0.25}/Mg_3(Al_{0.5})O$, 550 ^oC; (e) $Fe_{0.5}/Zn_3(Al_{0.5})O$, 450 ^oC; (f) $Fe_{0.5}/Zn_3(Al_{0.5})O$, 550 ^oC.

1-Phenylethanol: (g) $Fe_{0.25}$–$Co_{0.25}/Mg_3(Al_{0.5})O$, room temperature; (h)

$Fe_{0.25}$–$Co_{0.25}/Mg_3(Al_{0.5})O$, 100 °C.

Acetophenone: (i) $Fe_{0.25}$–$Co_{0.25}/Mg_3(Al_{0.5})O$, room temperature; (h) $Fe_{0.25}$–$Co_{0.25}/Mg_3(Al_{0.5})O$, 100 °C.

Figure 10. FTIR spectra of pyridine adsorbed on $Fe_{0.5}/Mg_3(Al_{0.5})O$, $Fe_{0.25}$–$Co_{0.25}/Mg_3(Al_{0.5})O$ and $Fe_{0.5}/Zn_3(Al_{0.5})O$ catalysts.

a) $Fe_{0.25}$–$Co_{0.25}/Mg_3(Al_{0.5})O$, 100 °C; b) $Fe_{0.25}$–$Co_{0.25}/Mg_3(Al_{0.5})O$, 400 °C; c) $Fe_{0.5}/Mg_3(Al_{0.5})O$, 100 °C; d) $Fe_{0.5}/Mg_3(Al_{0.5})O$, 400 °C; e) $Fe_{0.5}/Zn_3(Al_{0.5})O$, 100 °C; f) $Fe_{0.5}/Zn_3(Al_{0.5})O$, 400 °C.

Scheme 1. Adsorption of 1-phenylethanol and acetophenone on $Fe_{0.25}$–$Co_{0.25}/Mg_3(Al_{0.5})O$.

Scheme 2. Plausible reaction scheme of ethylbenzene dehydrogenation on $Fe_{0.25}$–$Co_{0.25}/Mg_3(Al_{0.5})O$.

Figure 1. K. Takehira et al.

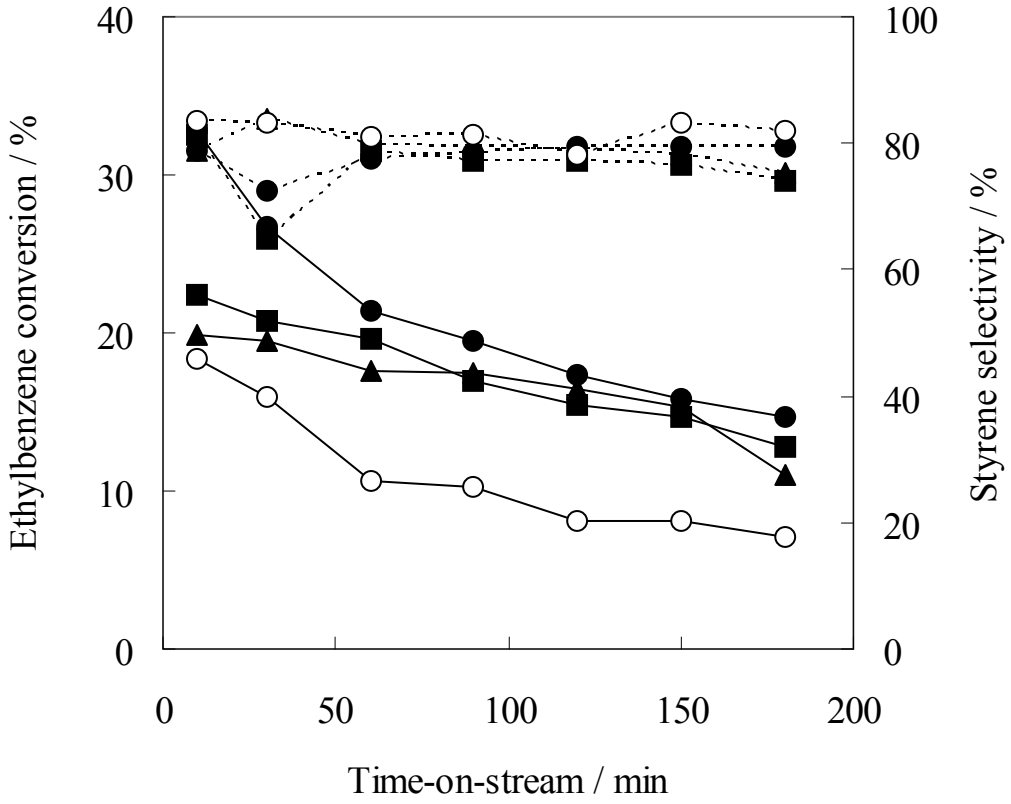

Figure 2. K. Takehira et al.

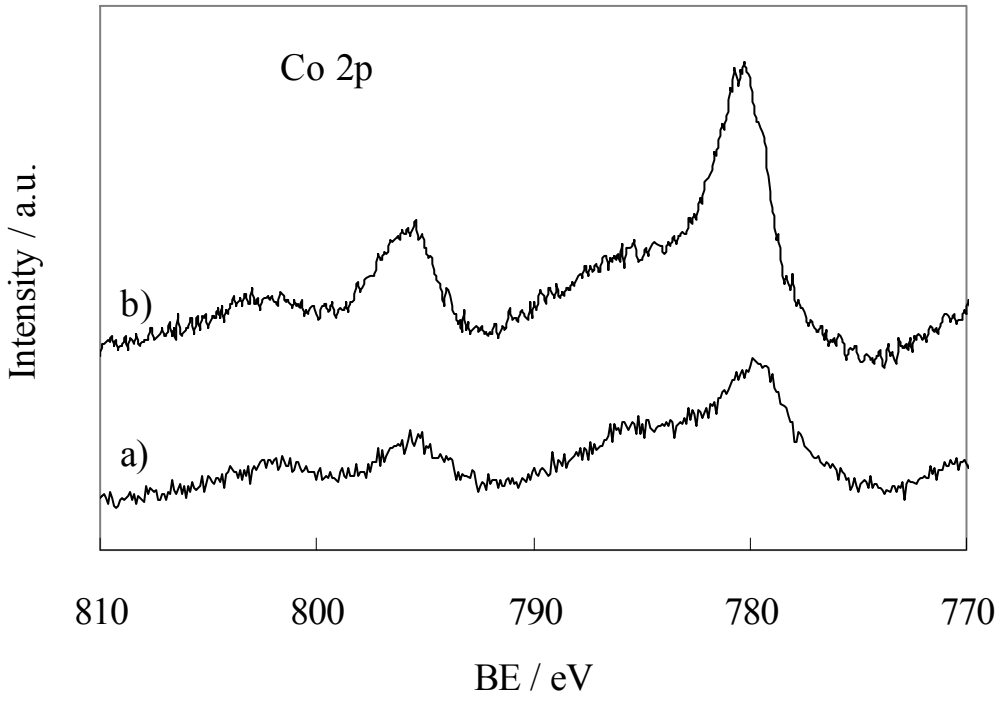

Figure 3. K. Takehira et al.

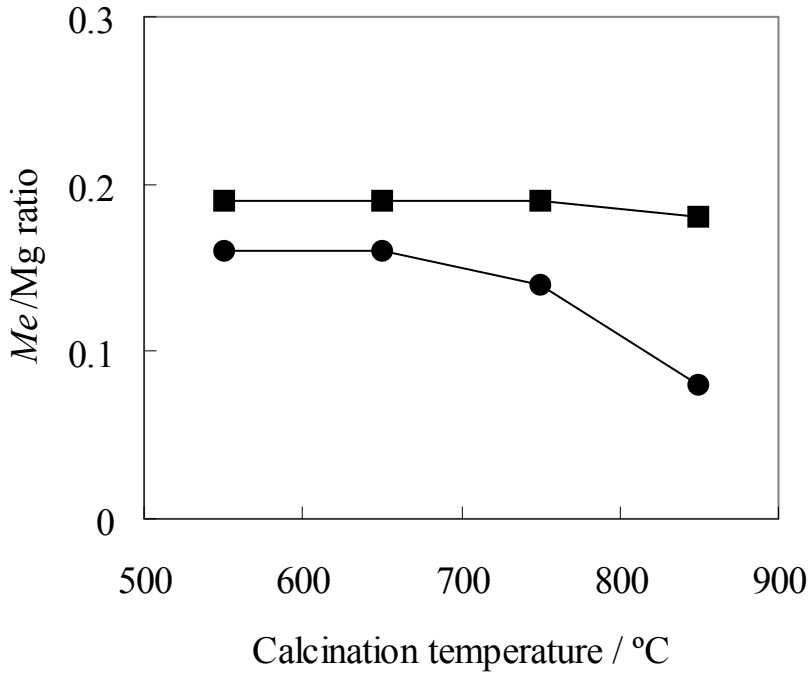

Figure 4. K.Takehira et al.

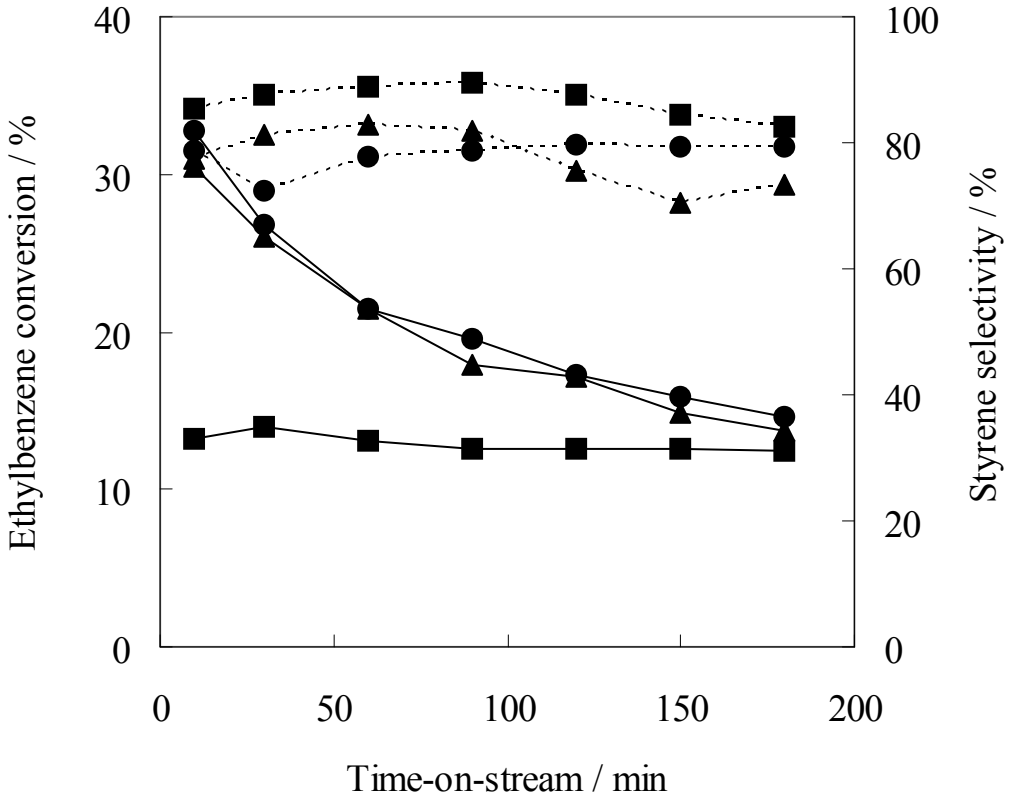

Figure 5. K. Takehira et al.

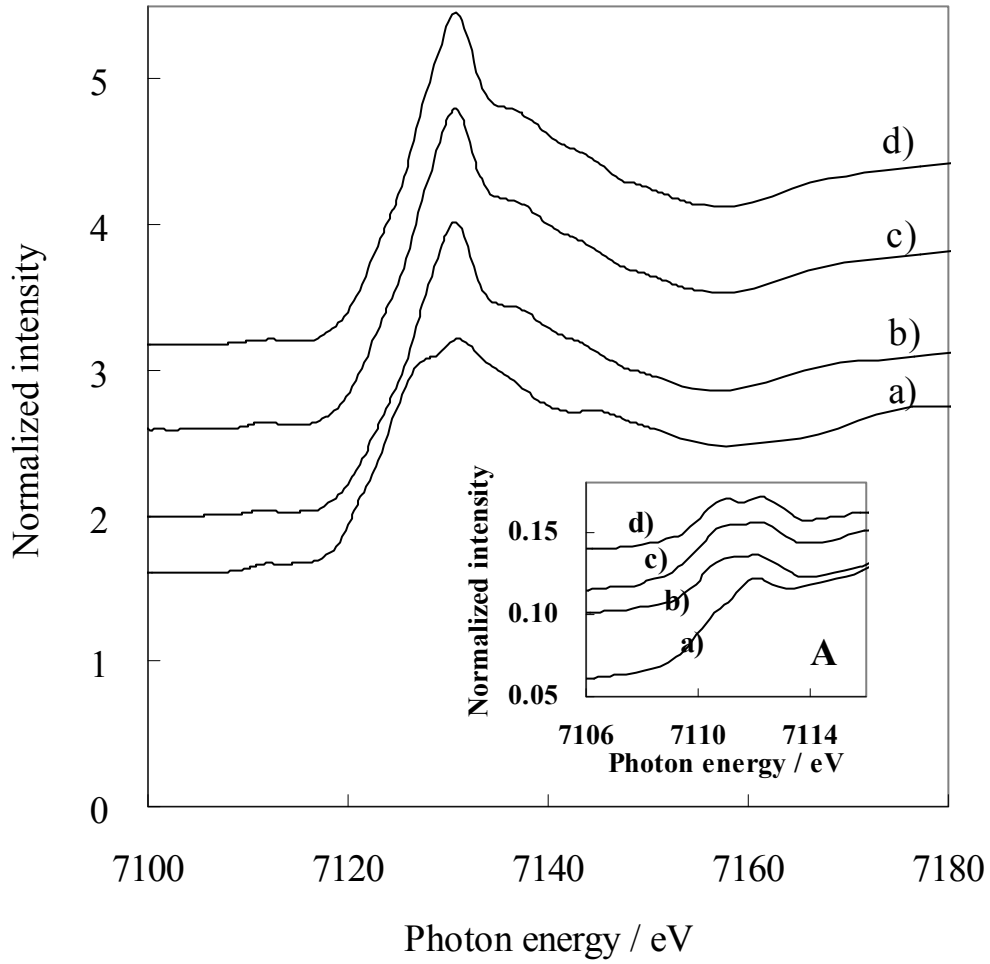

Figure 6. K. Takehira et al.

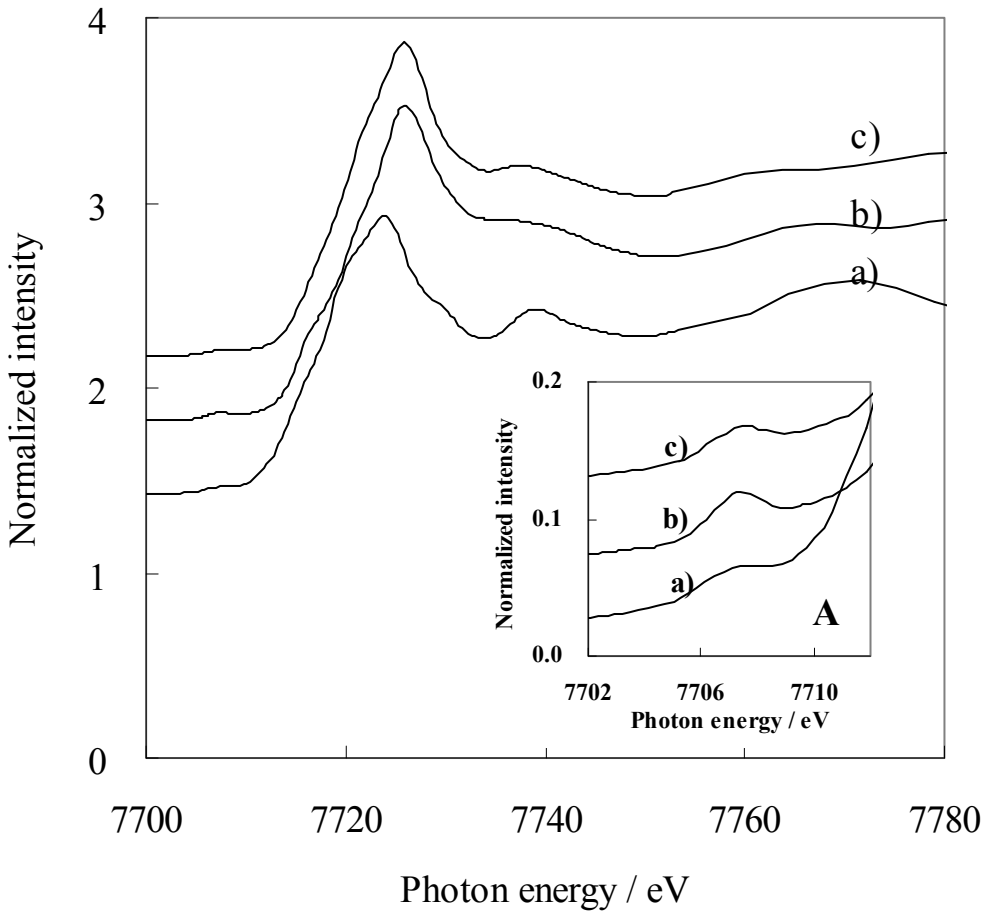

Figure 7. K. Takehira et al.

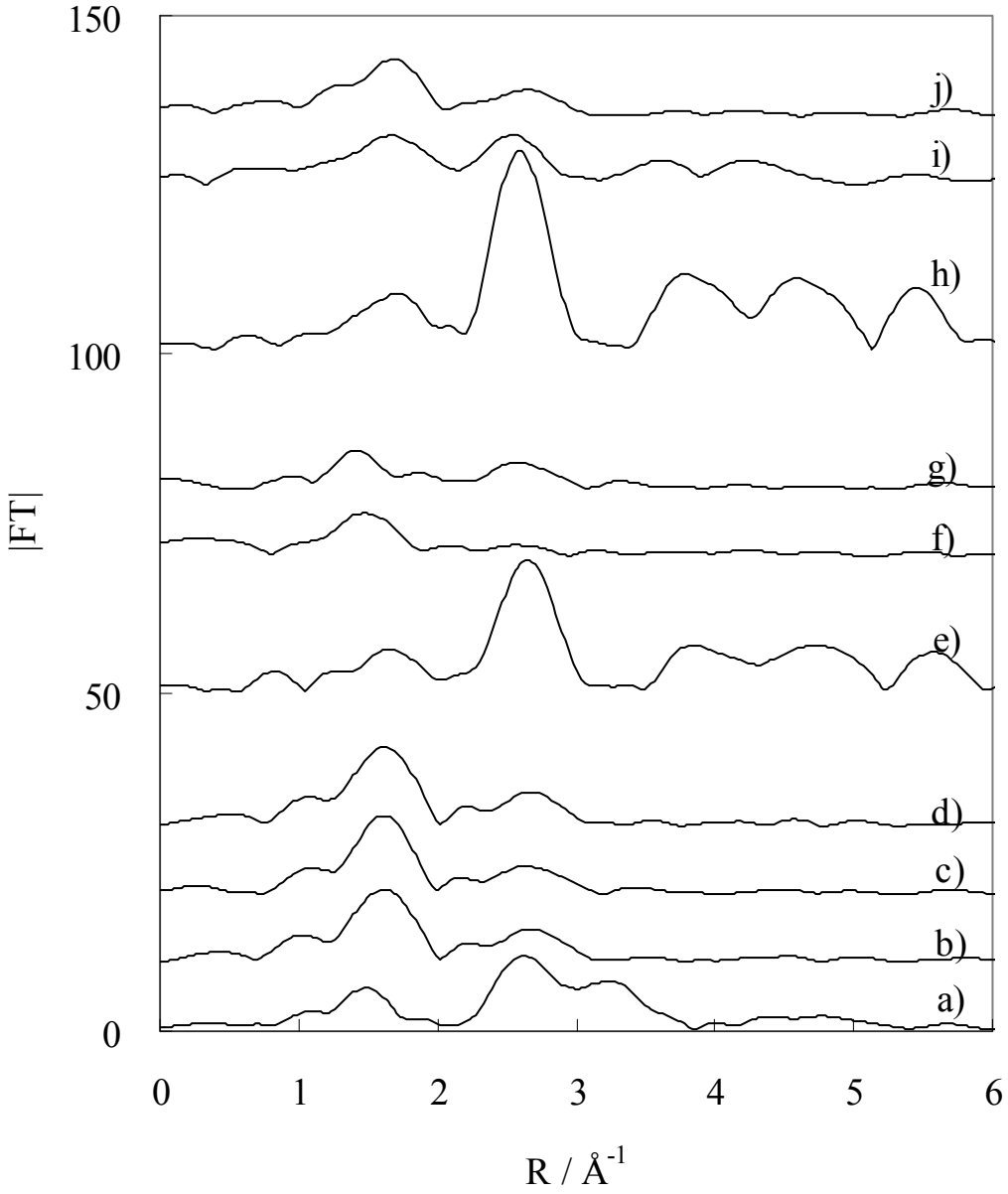

Figure 8. K. Takehira et al.

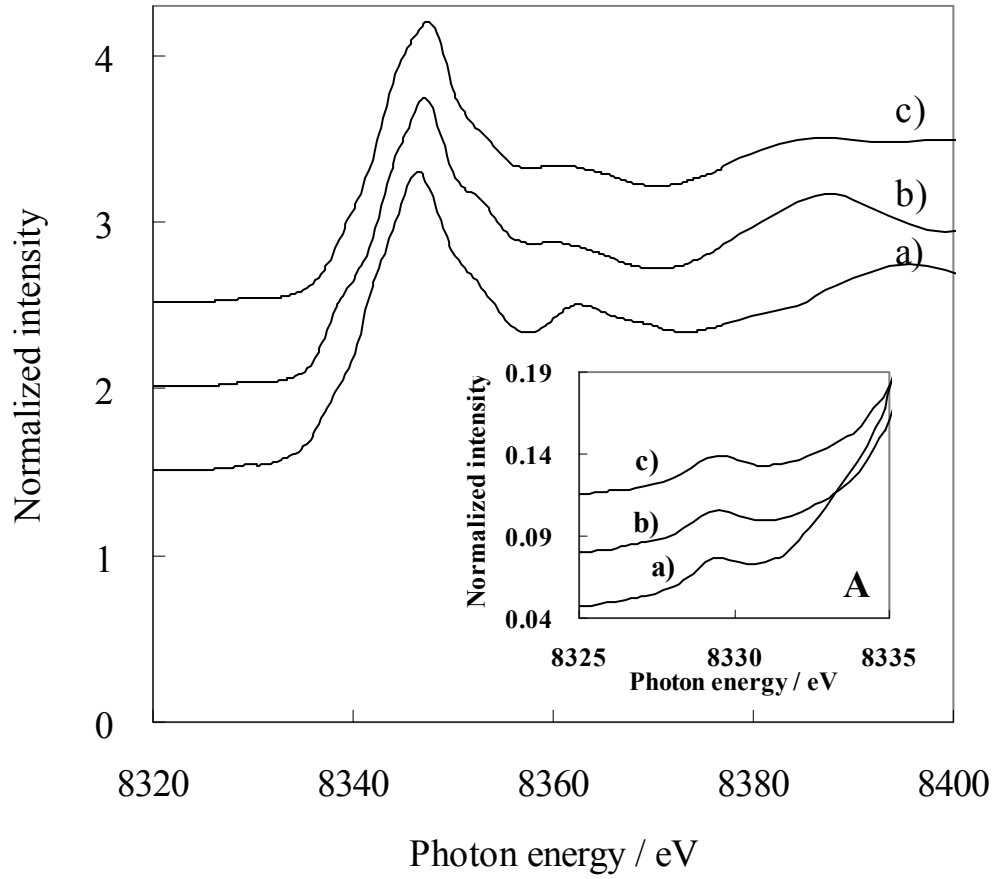

Figure 9. K. Takehira et al.

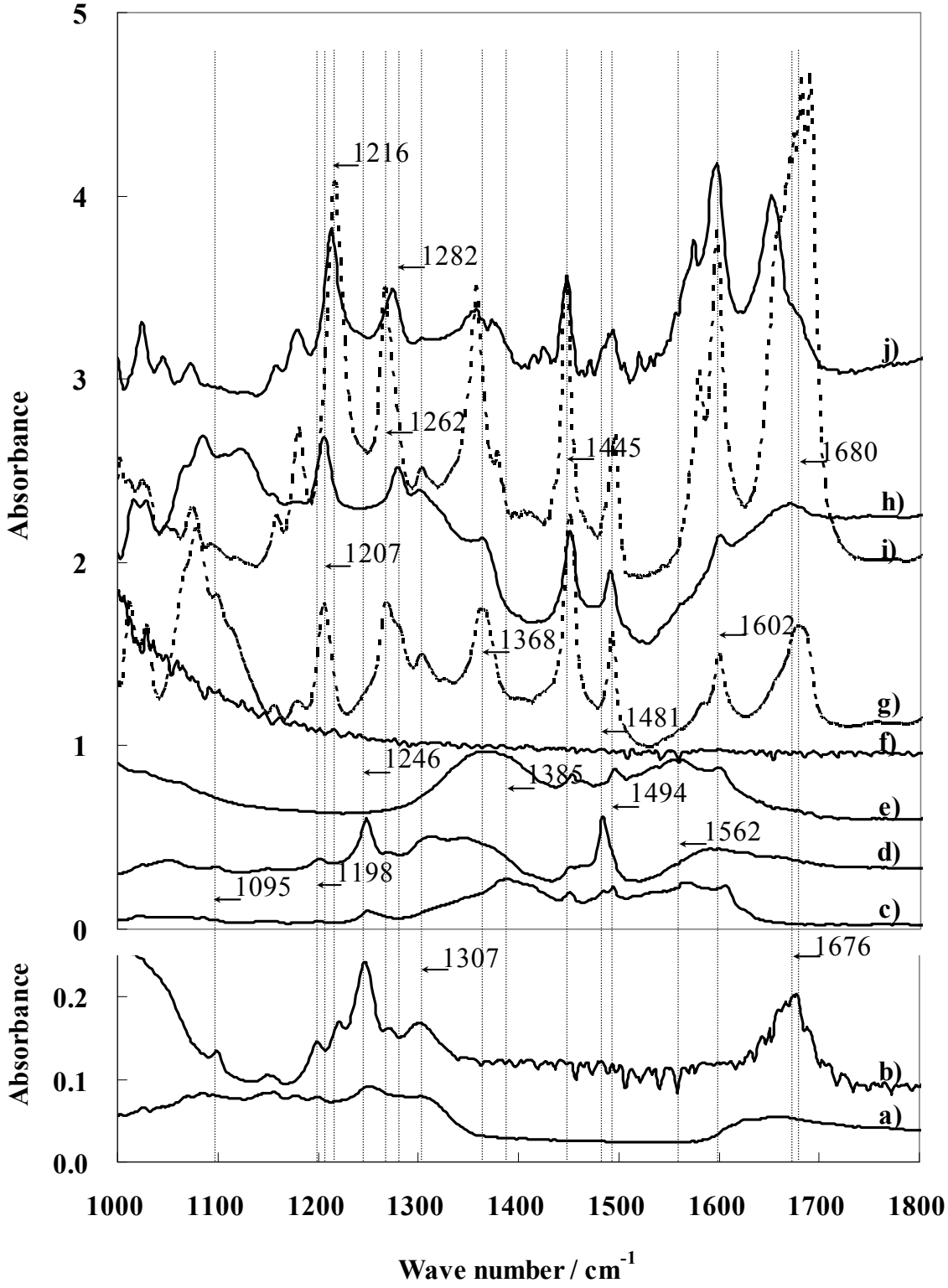

Figure 10. K. Takehira et al.

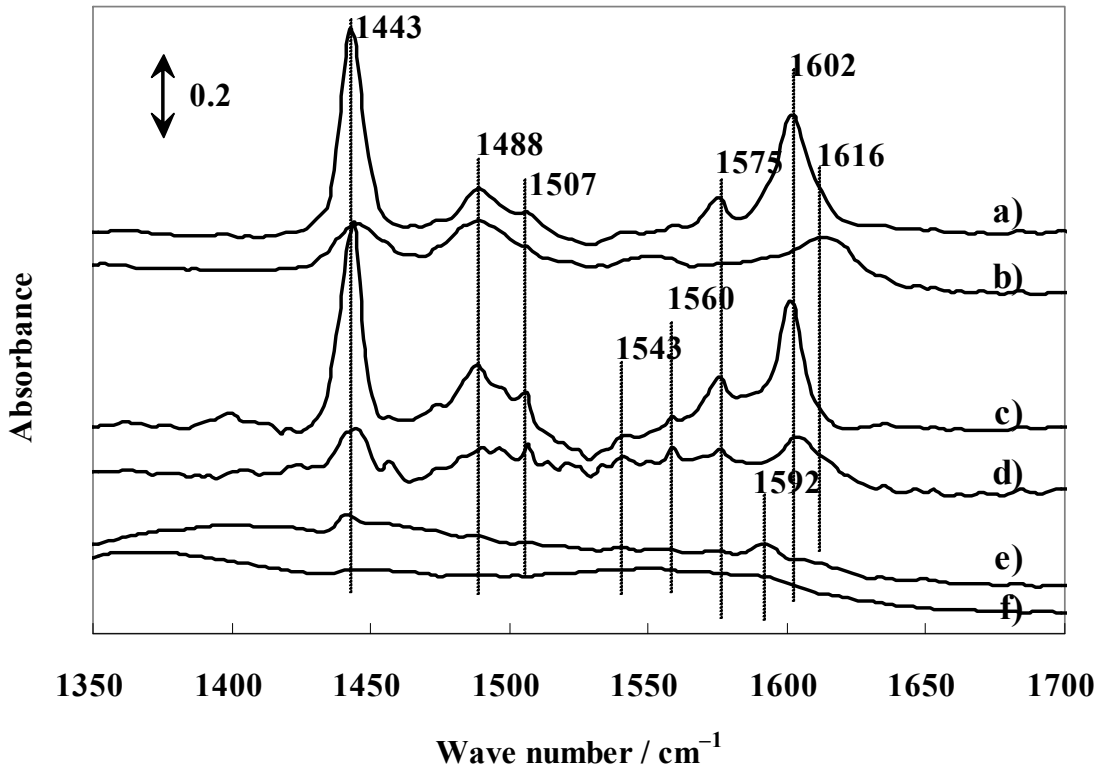

Scheme 1.

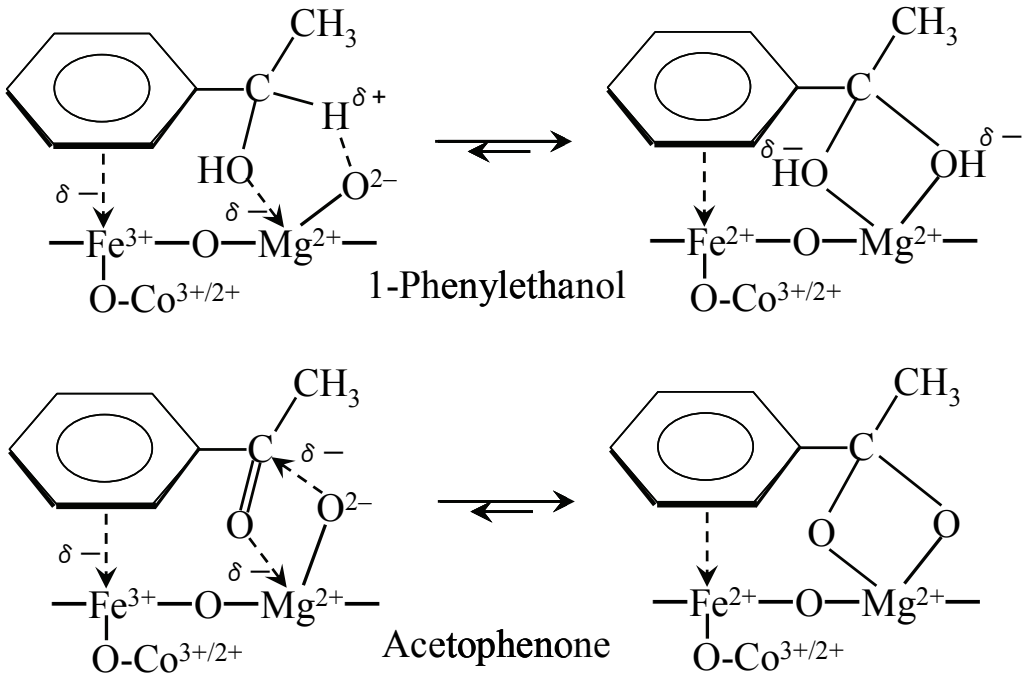
CH3
C
H
δ +
HO
O2–
δ –
δ –
Fe3+—O—Mg2+
O-Co3+/2+
1-Phenylethanol
CH3
C
δ –
HO
OH
δ –
Fe2+—O—Mg2+
O-Co3+/2+
CH3
C
δ –
O
O2–
δ –
δ –
Fe3+—O—Mg2+
O-Co3+/2+
Acetophenone
CH3
C
O
O
Fe2+—O—Mg2+
O-Co3+/2+

Scheme 2.

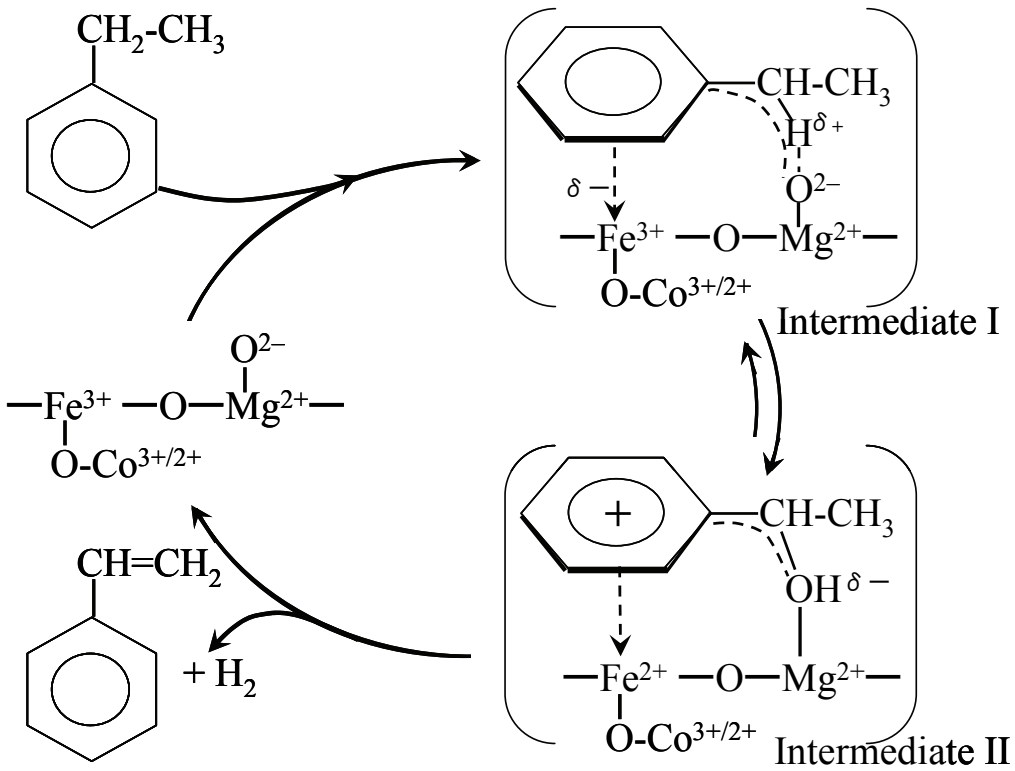
CH2-CH3
CH-CH3
Hδ+
δ −
O2−
—Fe3+ —O—Mg2+—
O-Co3+/2+
Intermediate I
O2−
—Fe3+ —O—Mg2+—
O-Co3+/2+
CH-CH3
OHδ −
CH=CH2
+ H2
—Fe2+ —O—Mg2+—
O-Co3+/2+
Intermediate II